Ultrafine CoSe nano-crystallites confined in leaf-like N-doped carbon for long-cyclic and fast sodium ion storage

Xiaodan Li [a, *], Wendi Zhang [a], Yi Feng [b], Wei Li [c], Peng Peng [d], Jianfeng Yao [b], Meicheng Li [d], Chunhai Jiang [a, **]

[a] Fujian Provincial Key Laboratory of Functional Materials and Applications, School of Materials Science and Engineering, Xiamen University of Technology, Xiamen 361024, China
[b] College of Chemical Engineering, Nanjing Forestry University, Nanjing, Jiangsu 210037, China
[c] Benjamin M. Statler College of Engineering & Mineral Resources, West Virginia University, Morgantown, WV 26506, USA
[d] State Key Laboratory of Alternate Electrical Power System with Renewable Energy Sources, North China Electric Power University, Beijing 102206, China

ABSTRACT

Considerable efforts have been devoted to developing sodium-ion batteries for large-scale energy storage due to the high abundance and low cost of sodium resources. However, the inferior cyclability and re-action kinetics of electrodes toward sodium ions still impedes their further development. In this study, we designed a two-dimensional (2D) composite where ultrafine CoSe nano-crystallites were confined in N-doped carbon (CoSe/NC-L) to attain excellent cycling performance and fast sodium ion storage. The CoSe/NC-L was successfully prepared through a high-temperature reaction of leaf-like Co-based ZIF (ZIF-L) and Se powder. It is demonstrated that the particle size of Se powder plays an important role in the formation of ultrafine CoSe nano-crystallites and encapsulated configuration. The combined merits of ultrafine CoSe and encapsulation into 2D NC matrix effectively enhance reaction kinetics, accommodate volume change expansion of CoSe and inhibit the formation of unstable SEI. Therefore, the CoSe/NC-L composite displayed high initial specific capacity of 530 mAh g^{-1} and Coulombic efficiency of 67.2% at 0.2 A g^{-1}. Notably, superior capacity retention of 82.2% with stable Coulombic efficiency of 97.0% is achieved at 0.5 A g^{-1} after 150 cycles in NaClO$_4$ electrolyte system. This work casts a new light on the smart design of metal selenide electrode materials for sodium ions batteries.

© 2018 Elsevier Ltd. All rights reserved.

1. Introduction

Lithium ion batteries (LIBs), as one of the most popular energy-storage power sources nowadays, have been widely used in portable electronic devices and electric vehicles [1,2]. However, the limited resources and high price of lithium hinder the further development of LIBs for large-scale energy storage [3]. In this context, sodium ion batteries (SIBs) have attracted worldwide attention due to the similar electrochemical property of sodium and lithium but high abundance and low cost of sodium resources. However, the ionic radius of Na$^+$ (~1.06 Å) is 40% larger than that of Li$^+$ (~0.76 Å), which leads to poor diffusion kinetics in the anode materials [4]. Thus, the design and synthesis of anode materials

with suitable morphology and proper pore structure for sodium ion batteries is highly necessary.

So far, various materials such as carbon materials [5,6], alloy materials [7,8], sulfides and selenides [9–13] have been synthesized and studied as anodes in terms of SIBs application. Among them, metal selenides exhibited higher volume capacity and rate performance than their oxides or sulfides counterparts due to the high volume density and low band gap [14,15]. Moreover, recent study has illuminated a distinctive phenomenon that the diffusion kinetics of sodium ion in Se nanowires was 4–5 times faster than that of lithium ion [16]. Theoretically, metal selenides possess extremely potential as high-performance anode materials for sodium ion batteries. However, large volume changes repeatedly proceed in metal selenides anodes during cycling, which arouses severe pulverization and unstable solid-state interphase (SEI), hence resulting in poor cycling stability and low coulombic effi-ciencies. Therefore, in order to realize the wide application of metal selenides in SIBs, the above-mentioned problems must be solved

* Corresponding author.
** Corresponding author.
E-mail addresses: xd_li@xmut.edu.cn (X. Li), chjiang@xmut.edu.cn (C. Jiang).

properly.

It was proposed that incorporating metal selenide with carbonaceous material could enhance the electronic conductivity, accommodate the volume change expansion and inhibit the formation of unstable SEI, thus maintaining the cycling stability [17—19]. In this respect, zeolitic imidazole frameworks (ZIFs) should be good candidates as precursor/template to design and fabricate the cobalt selenide/carbon hybrids anodes for SIBs [20—23]. ZIFs were easily converted into N-doped carbon materials via direct carbonization, endowing them with higher electronic conductivity and more active sites than pure carbon [24]. On the other hand, reducing the size of active materials was supposed to provide porosity/space to accommodate mechanical stress, shorten the sodium ion diffusion path and reduce the electrode polarization. At present, most studies on morphological regulation of metal selenide focused on the types of selenization and the application of surface additives [11,26,21,25]. However, the influences of selenium source size and selenization kinetics on the structure and composition of ZIF-derived cobalt-selenide/carbon composite are still unknown.

Recently, two-dimensional (2D) materials have stimulated great interests due to their unique and compelling properties absent in their counterparts [27,28]. Typically, 2D materials possess numerous active sites and short paths for ions diffusion, which are potential advantages for energy storage [29,30], especial for alkali ions storage. Nevertheless, the design of cobalt selenide/carbon materials derived from 2D ZIFs have been rarely reported for sodium ion storage. In this work, we designed a 2D composite where ultrafine CoSe nano-crystallites were confined in N-doped carbon (CN) for sodium ion storage. It was synthesized by the selenization treatment of a leaf-like Co-based ZIF (ZIF-L) using Se powder. The influence of selenization kinetics on the final composition and structure of cobalt selenide in NC matrix were firstly studied, which is an important direction for sodium ion storage performance. Finally, the optimized 2D CoSe/NC-L composite exhibited excellent sodium storage capacity of 397 mAh g^{-1} after 150 cycles at 0.5 A g^{-1}. Even at 5 A g^{-1}, the capacity of the 2D CoSe/NC-L composite was still as high as 330 mAh g^{-1}.

2. Experimental section

2.1. Material synthesis

Preparation of ZIF-L: In a typical synthesis, 0.59 g of Co(NO$_3$)$_2$· 6H$_2$O was dissolved in 40 ml of deionized water, forming solution A after stirring for 10 min. Similarly, solution B was formed by dissolving 1.3 g of 2-methylimidazole into 40 ml of deionized water. Then, the solution A was slowly poured into solution B under continuous stirring, and aged for 4 h at room temperature. Lastly, the violet product was collected by centrifugation and washed with water for 3—5 times, and freeze-dried overnight.

Preparation of nano-sized Se: In a typical procedure, 52 mg Na$_2$SeO$_2$ and 200 mg glucose were dissolved into 30 ml deionized water. After stirring for 20 min, the mixture solution was transferred into a 35 ml Telfon-lined stainless steel autoclave and placed in an electric oven at 95 °C for 12 h. The gray precipitate was collected by centrifugation and washing with water several times, followed by vacuum drying at 60 °C for overnight.

Preparation of CoSe/NC-L: The as-prepared ZIF-L and nano-sized Se were mixed with a mass ratio of 1:1, and the mixture was placed into a tube furnace with a ceramic boat. The mixture powder was treated at 650 °C for 3 h in N$_2$ atmosphere with a heating rate of 1 °C min^{-1} to obtain CoSe/NC-L composite.

Preparation of CoSe$_x$/NC-L: The as-prepared ZIF-L and commercial micro-sized Se were mixed with a mass ratio of 1:1, and the

following procedures is the same as above.

For comparison, ZIF-67 polyhedral was prepared in 52 ml of methanol and the corresponding CoSe$_x$/CN polyhedral was obtained by using micro-sized Se. Other synthesis conditions were identical with the preparation of CoSe$_x$/NC-L.
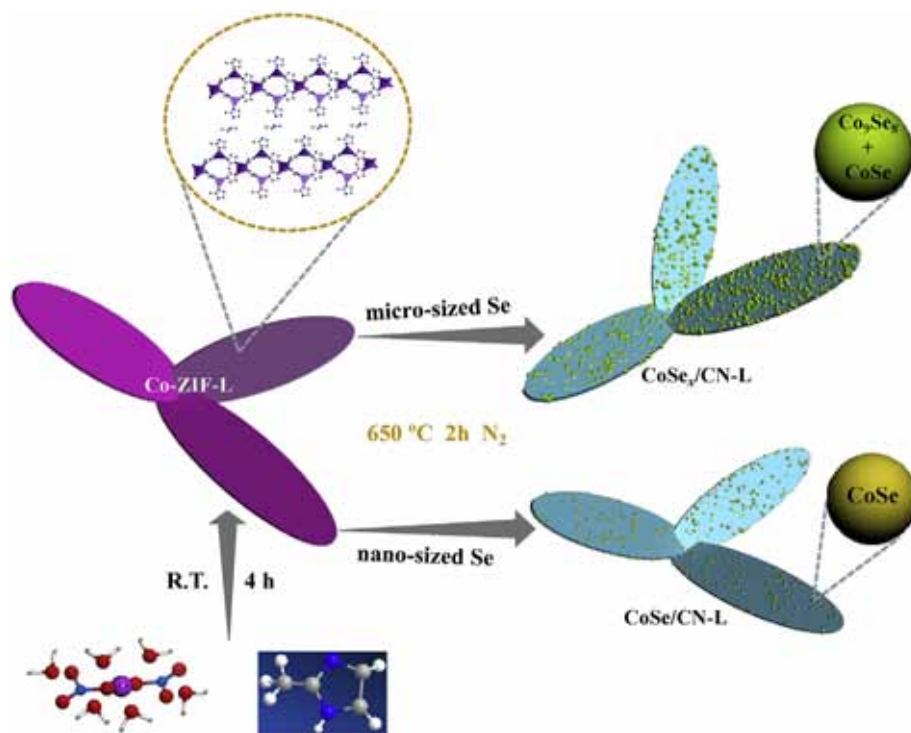
2.2. Characterization

Scanning electron microscopy (SEM) (Zeiss Sigma 500) was employed to characterize the size, distribution and morphology of the as-prepared samples. TEM and HRTEM measurements were conducted on FEI Talos 200s microscope equipped with a high-precision EDX spectroscopy detector. The chemical composition analysis were performed by XRD (MiniFlex 600, Cu-Ka radiation) and XPS (ESCALAB 250Xi, ThermoFisher, UK, Al Ka radiation). TG analysis was performed on a NETZSCH TG203F instrument under a heating rate of 5 °C min^{-1} in air atmosphere. FTIR spectra were obtained by Nicolet 380. The porosity of as-prepared samples was measured by nitrogen adsorption-desorption isotherms on Quantachrome at 77 k. Raman spectra were collected using a LabRAM system with 532 nm laser excitation.

2.3. Electrochemical measurements

The working electrodes were prepared by coating slurry onto a copper foil. The slurry is a mixture of 70 wt% of active materials (CoSe/NC-L, CoSe$_x$/CN-L, or CoSe$_x$/CN-Polyhedral), 20 wt% of conductive agent (Super-P), and 10 wt% of binder (1% sodium alginate solution) in water. Then the samples were dried at 100 °C in vacuum for 12 h before pressing. In an Ar-filled glovebox (MBRAUN, Germany), the as-prepared electrodes, counter electrode (Na metal slice), and a separator (fiberglass, Whatman) were assembled into a standard CR2032-type coin cell. The electrolyte was 1.0 M NaClO$_4$ dissolved in a mixture of ethylene carbonate (EC) and dimethyl carbonate (DMC) (v/v = 1:1) with 5.0% fluoroethylene carbonate (FEC). The cells were aged overnight prior to the electrochemical measurements. The battery cycling and rate tests were conducted in the voltage window of 0.1—3.0 V on a multichannel battery tester (Land Instruments, China). Cyclic voltammetry (CV) profiles were recorded on an electrochemical workstation (PARSTAT™ MC, AMETEK, USA). Electrochemical impedance spectra (EIS) were investigated by employing an AC voltage of 10 mV amplitude over the frequency range from 100 kHz to 0.1 Hz. The specific capacities were calculated based on the total active materials. The mass loading of active electrode material was ~0.9 mg cm^{-2}.

3. Results and discussion

The fabrication procedures of CoSe/NC-L composites and CoSe$_x$/NC-L hybrids are described in Scheme 1. Firstly, leaf-like Co-containing zeolite frameworks, ZIF-L, were synthesized by a facile solution approach in air at room temperature. The ZIF-L sample was composed of two-dimensional leaves with thickness of tens of nanometers and plane size ranging from 0.5 to 2 μm (Fig. 1a). Then, the as-prepared ZIF-L served as the precursor to react with Se powder at 650 °C under nitrogen protection. During the selenization process, the Co^{2+} in ZIF-L suffered from in-situ reaction with Se source to form selenide cobalt and organic ligands were carbonized into nitrogen-doped carbon matrix (NC), maintaining the original two-dimensional leaf-like architecture. In order to investigate the effect of selenization kinetics on the structure and composition of selenide cobalt/NC products, nano-sized Se was synthesized by a simple solution method (Fig. S1). The as-prepared nano-sized Se and commercial micro-sized Se were used as Se sources for the

Scheme 1. Illustration of the fabrication process of the CoSe/NC-L composite and CoSe$_x$/NC-L hybrids.
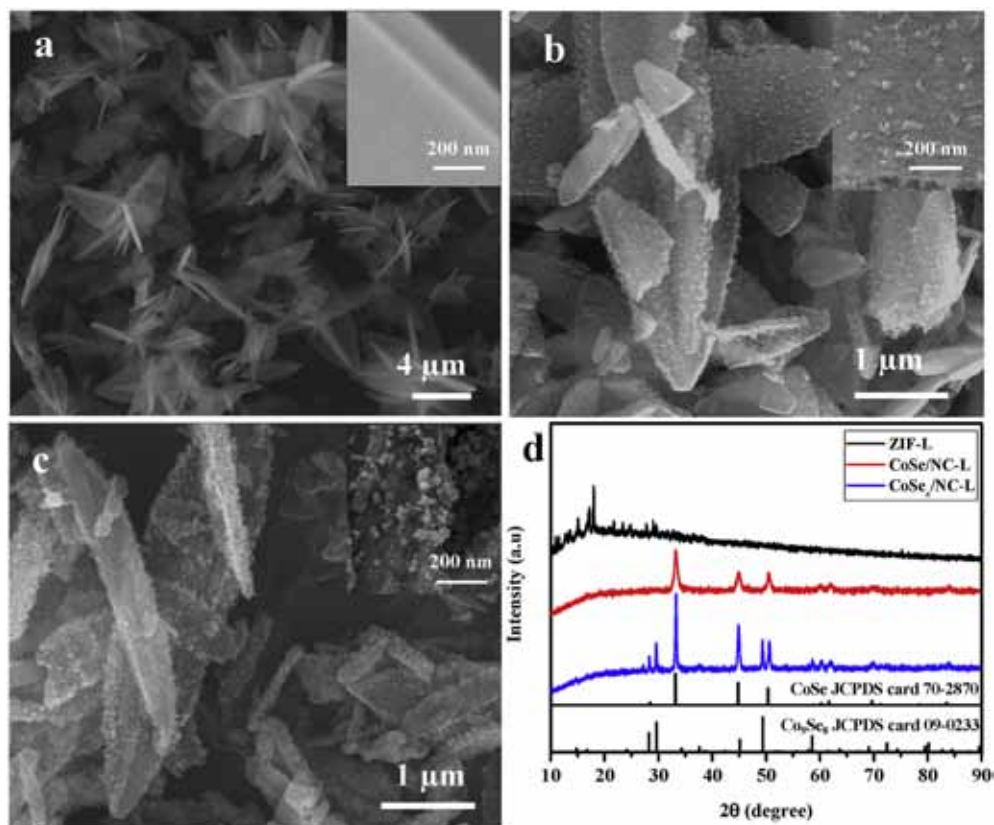
Fig. 1. Composition and morphology characterization. a) SEM images of ZIF-L precursor. b) SEM images of CoSe/NC-L. c) SEM images of CoSe$_x$/NC-L d) XRD patterns of ZIF-L, CoSe/NC-L, CoSe$_x$/NC-L and standard patterns of JCPDS Cards. Insets: high-magnification images of the corresponding surface.

selenization process, respectively.

The scanning electron microscope (SEM) images in Fig. 1b presents the reaction products derived from ZIF-L and nano-sized Se (Fig. S1a), CoSe/NC-L composites, in which ultrafine nanoparticles sparsely distribute on the surface of leaf-like NC matrix. According to the XRD pattern (Fig. 1d, red line), the ultrafine nanoparticles are indexed by freboldite CoSe and the NC matrix is likely to be amorphous carbon due to the absent carbon characteristic peak. While using micro-sized Se source (Fig. S1b), it tends to produce more serried and coarsened particles on the surface of NC matrix (Fig. 1c). And the XRD pattern of this sample is corresponding to a mixture of CoSe and Co_9Se_8, thus it is named as $CoSe_x$/NC-L hybrids (Fig. 1d, blue line). Moreover, the XRD pattern of CoSe/NC-L composites show weaker and broader peaks than that of $CoSe_x$/NC-L hybrids, further confirming the easier formation of ultrafine CoSe nano-crystallites by employing nano-sized Se source. Their crystallite size can be calculated by Scherer equation:

$$D = \frac{k\lambda}{\beta \cos\theta} \tag{1}$$

Where D is the average grain size, k means the Scherer constant (a value of ~0.9), λ is equal to 1.54 Å, β is the full width at half maximum (FWHM) of the diffraction peaks and θ is the corresponding angle of diffraction. The calculated results show that the crystallite size of CoSe in CoSe/NC-L is 11.2 nm while that of CoSe/Co_9Se_8 in $CoSe_x$/NC-L is 30.9 nm. According to the size distribution in Fig. S1d, the as-prepared nano-sized Se exhibits better uniformity and smaller particle size than that of commercial micro-sized Se. The nanometer size effect endows nano-sized Se with faster dynamics of phase transformation (melting/vaporization) and diffusion kinetics, which is favorable for rapid nucleation and complete selenization reaction. Thus, nano-sized Se results in the formation of ultrafine CoSe nanoparticles rather than coarsened CoSe/Co_9Se_8 particles embedded in NC matrix.

The detailed structural information of CoSe/NC-L has been further analyzed by transmission electron microscopy (TEM). As shown in Fig. 2a and b, a two-dimensional leaf-like structure could be observed clearly, indicating that the in-situ growth of CoSe nanoparticles did not damage the leaf-like morphology of N-doped carbon matrix. The high-resolution TEM (HRTEM) image (Fig. 2c) reveals that the ultrafine CoSe nanoparticles have a diameter of 10 nm and are mostly encapsulated into N-doped carbon matrix. The carbon matrix exhibits long-range disorder of amorphous phase, while the nanoparticles display the lattice fringes with a spacing of 0.27 nm (Fig. 2d), corresponding to the (101) plane of freboldite CoSe. This is consistent with the XRD results. In addition, an energy-dispersive X-ray (EDX) elemental mapping reveals the distribution of Co, Se, C and N, where Se and Co in pairs throughout the leaf-like matrix with uniformly dispersed N and C. The results had been further confirmed by the intermittently increased Co/Se signals and steady C/N signals in EDX linescan profiles (Fig. 2e). Thus, CoSe/NC-L composites present two-dimensional leaf-like architecture that can provide plentiful active sites for sodium ions storage, and the flexible amorphous carbon matrix would accommodate the volume change of CoSe nano-crystallites.

The surface functional groups and chemical states of elements on the surface of CoSe/NC-L composites and $CoSe_x$/NC-L hybrids were investigated by Fourier transform infrared spectroscopy (FTIR) and X-ray photoelectron spectroscopy (XPS). As shown in Fig. S2, a series of sharp peaks are assigned to the stretching vibration of C—N, C=N, C—H and N—H [31,32]. These abundant nitrogen-containing species are indications of nitrogen doping in CoSe/NC-L and $CoSe_x$/NC-L. The high-resolution XPS spectrum of C 1s (Fig. S3a,c) demonstrates that the peaks at 284.5, 285.6, and 286.8 eV originate from sp2-bonded C—C, C—N, and C—O, respectively [27,33]. The presence of C—N peak reveals that the nitrogen is well doped in the carbon matrix. The state of N element was further
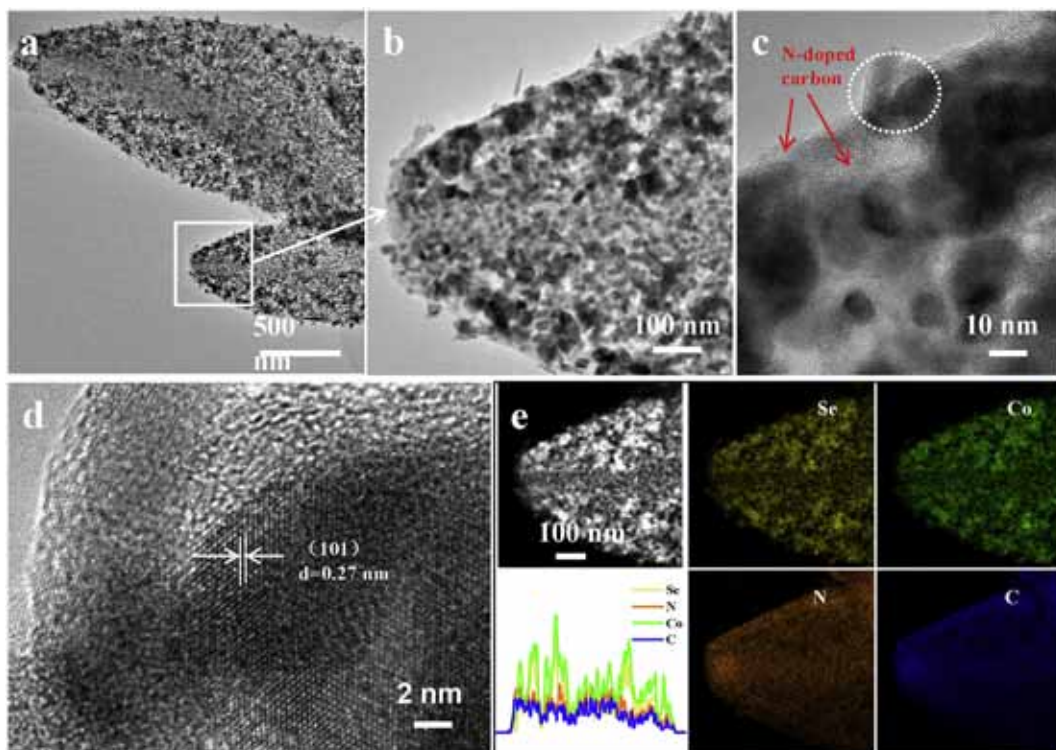

Fig. 2. Detailed structural characterization. a, b) TEM images of CoSe/NC-L. c, d) HRTEM images of CoSe/NC-L and e) the EDX linescan profiles and mapping images of Se, Co, N and C.

studied by the N 1s spectrum in Fig. S3b, d, where three types of nitrogen atoms at binding energies of 398.2, 399.1, and 400.7 eV are corresponding to pyridinic N, pyrrolic N, and graphitic N, respectively [20,34]. The nitrogen contents of CoSe/NC-L, especially the proportion of pyridinic N and pyrrolic N, are higher than those of $CoSe_x$/NC-L (Table S1). Generally, pyridinic N and pyrrolic N promote local disorder and defect sites, leading to an enhanced carrier transport in CoSe/NC-L composite. In the high-resolution Co 2p spectrum of CoSe/NC-L (Fig. 3a), two pairs of peaks located at around 796.4 eV/792.9 eV for Co 2p 1/2 and 780.6 eV/778.0 eV for Co 2p 3/2 are ascribed to the spin-orbit characteristic of Co^{2+} and Co^{3+} [35—38]. Comparatively, Co 2p peaks of $CoSe_x$/NC-L containing Co_9Se_8 (Fig. 3c) shift towards the higher binding energy, indicating different valence states and ion distribution between different Se surroundings of Co [38]. As for the high-resolution spectrum of Se 3d, the two peaks at 53.5 and 54.4 eV (Fig. 3b, d) are corresponding to the binding energies of Se 3d5/2 and Se 3d3/2 in cobalt selenide, respectively [17,39], while the peaks at 58—60 eV are attributed to Se—O bonds at the surface and Co 3p [40]. Obviously, the contrast between the two peak intensities demonstrates that the selenation degree of $CoSe_x$ is less than that of CoSe and the coarsened particles exposed to matrix suffer from possible oxidation. This may bring out adverse impact on Na^+ storage performance since selenium dominates the electrochemical reaction with sodium. As shown by the TG curves in Fig. S4a, the weight loss below 200 °C is mainly attributed to the evaporation of water molecules, and the slight weight increase at about 320 °C implies the oxidation of cobalt and selenium species [21,41]. Thereafter, a dramatic weight loss occurs

due to the combustion of CN matrix and the escape of selenium oxide [26,42]. Particularly, the combustion process of $CoSe_x$/CN-L hybrid begins later, which illustrates the slower oxidation reaction of coarsened $CoSe_x$; whereas, the combustion process of CoSe/NC-L composite lasts longer time, deducing that ultrafine CoSe nanocrystalline wrapped into CN matrix improves the structural stability of CoSe/NC-L composite. Finally, the residual weights of the two samples are approximate, indicating their similar Co contents due to the same precursor. The XRD pattern of the fine product after TG analysis is assign to Co_3O_4 (Fig. S4b). Based on the invariant Co atom during reaction [20,22], the estimated content of CoSe in CoSe/NC-L composite is about 72.8 wt%.

Nitrogen adsorption-desorption measurements were employed to characterize the specific surface area and porosity of CoSe/NC-L and $CoSe_x$/NC-L. As shown in Fig. 4, these adsorption-desorption isotherms are assigned to a type-IV curve with a H3 hysteresis loop, indicating the present of mesoporous structure in the samples [43,44]. The specific surface area of CoSe/NC-L and $CoSe_x$/NC-L are calculated to be 140.9 $cm^2\,g^{-1}$ and 136.1 $cm^2\,g^{-1}$, respectively, according to the Brunauer-Emmett-Teller (BET) method. Fig. 4c compares the corresponding pore size distributions of the two samples obtained from the Barrett-Joyner-Halenda (BJH) model. The CoSe/NC-L composite presents more pores of 2—10 nm due to the ultrafine CoSe particles in matrix. As for $CoSe_x$/NC-L, the excessive growth of coarse $CoSe_x$ particles needs to occupy spaces, resulting in reduced pores between the particles. Fig. 4d displays the Raman spectra of CoSe/NC-L and $CoSe_x$/NC-L, where D peak indicates the disorders or defects in the carbon matrix, and G peak
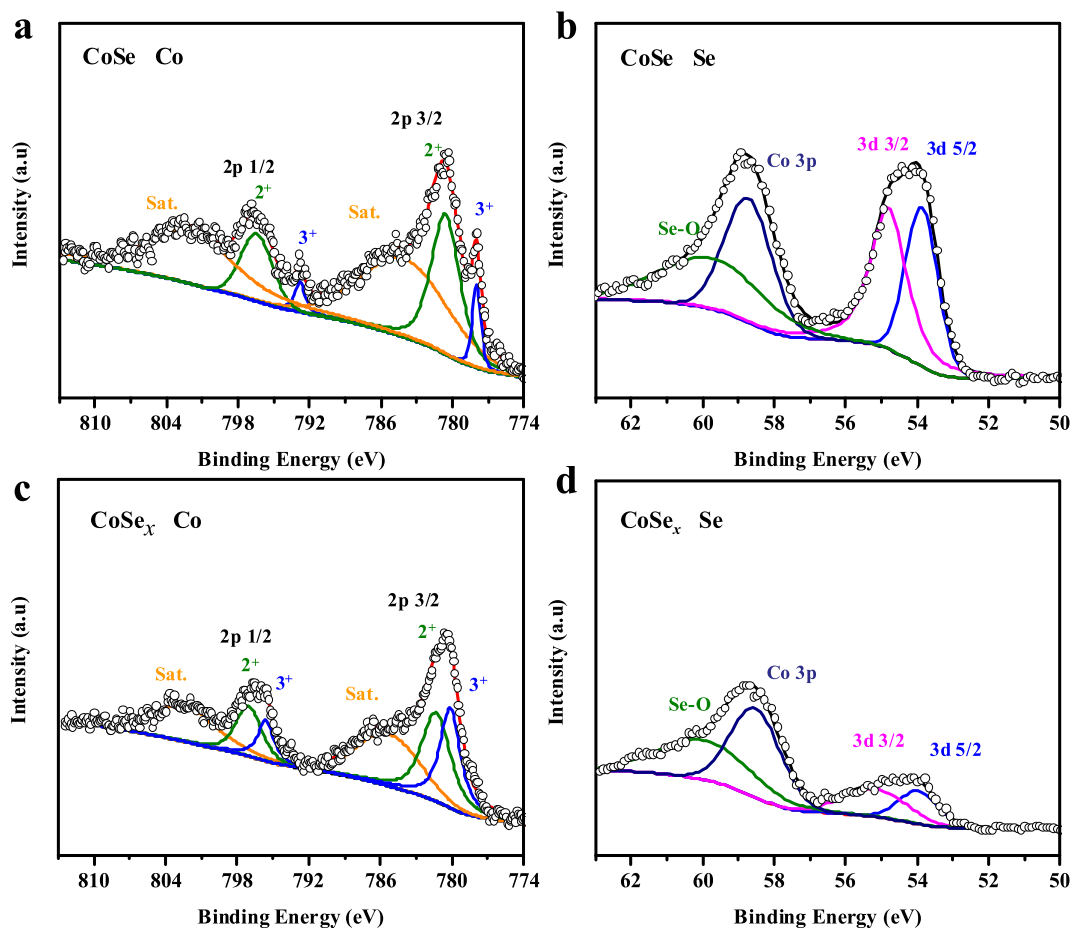

Fig. 3. XPS spectra of as-prepared samples. a) Co 2p peak of CoSe/NC-L, b) Se 3d peak of CoSe/NC-L, c) Co 2p peak of $CoSe_x$/NC-L, and d) Se 3d peak of $CoSe_x$/NC-L.
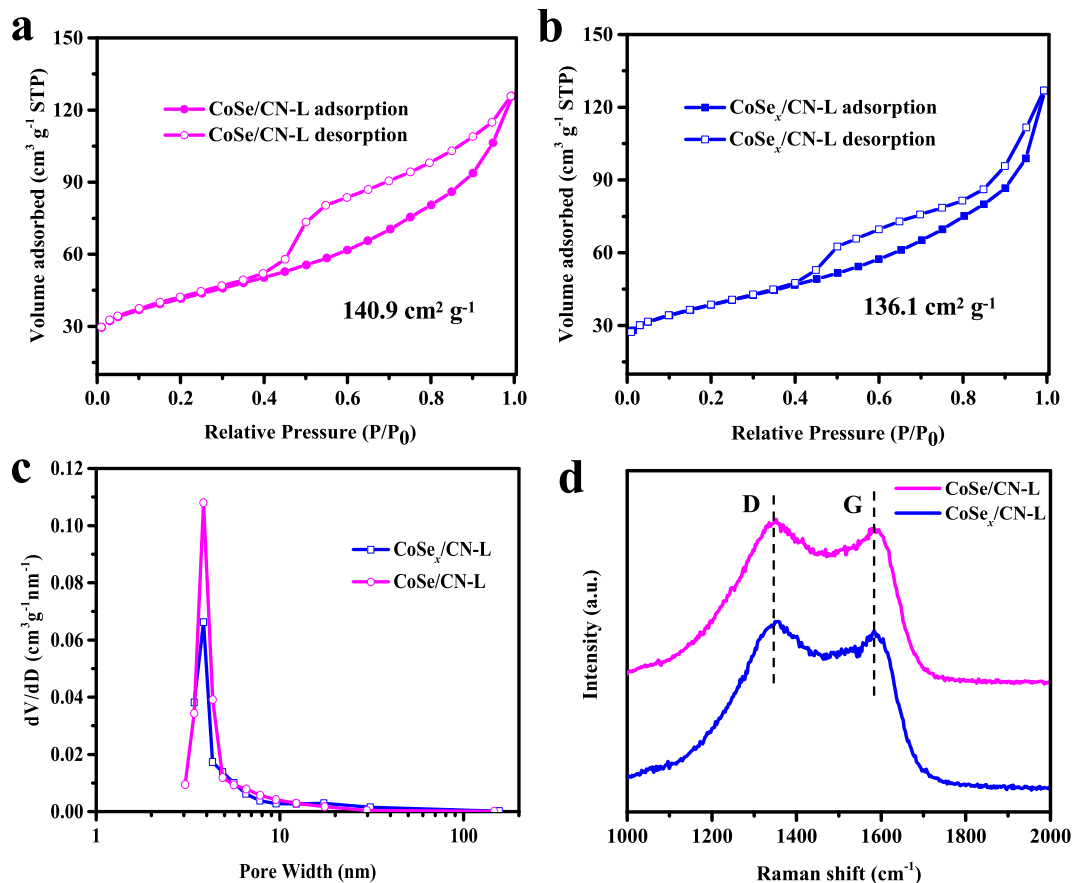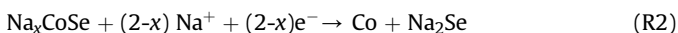
Fig. 4. Nitrogen adsorption-desorption isotherms of a) CoSe/NC-L and b) CoSe$_x$/NC-L. c) Corresponding pore size distributions of the two samples. d) Raman spectra of CoSe/NC-L and CoSe$_x$/NC-L.

originates from the graphitized carbon. Accordingly, we had fitted the spectra by Gaussian and the integrated areas [31] of these curves were exhibited in Fig. S5. The value of I_D/I_G for CoSe/NC-L and CoSe$_x$/NC-L are about 0.98 and 0.95, respectively. It reveals that the carbon marix of CoSe/NC-L possesses slightly more defects than that of CoSe$_x$/NC-L, leading to enhanced sodium ions storage.

The CoSe/NC-L composite was then assembled into batteries with Na metal as counter electrode to evaluate the electrochemical performance. The cyclic voltammetry (CVs) curves of CoSe/NC-L electrode was collected at a scan rate of 0.1 mV s^{-1} between 0.1 V and 3 V versus Na$^+$/Na. Fig. 5a presents the results for the first five scans. During the initial scan process, CoSe/NC-L electrode presents two cathodic peaks at respectively ~1.55 V, ~0.72 V and one anodic peak at ~1.82 V. The weak cathodic peak at 1.55 V is associated with the intercalation of Na ions into the CoSe, resulting in the formation of Na$_x$CoSe (Reaction (1)) [14,20]. The strong cathodic peak at 0.72 V is due to the further reduction of Na$_x$CoSe to Na$_2$Se and metallic Co (Reaction (2)), and the formation of a solid-state interphase (SEI) layer [20,21]. And the anodic peak at ~1.82 V is assigned to the reversible conversion reactions of Na$_2$Se and Co to CoSe [17]. The electrochemical reactions of the CoSe/NC-L composite during the first discharge/charge processes occur as follows:

$$CoSe + xNa^+ + xe^- \rightarrow Na_xCoSe \qquad (R1)$$

$$Na_xCoSe + (2\text{-}x)\,Na^+ + (2\text{-}x)e^- \rightarrow Co + Na_2Se \qquad (R2)$$

In subsequent cycle, the cathodic peaks observably shift to 1.07 V and 1.26 V vs Na/Na$^+$ due to the irreversible phase transition

[18]. Meanwhile, the identified anodic/cathodic peaks exhibit favorable repeatability, implying the good electrochemical stability of CoSe/NC-L composite for Na$^+$ storage. Fig. 5b reveals the GDC voltage curves of CoSe/NC-L composite at a current density of 0.2 A g^{-1}. The reaction processes in these GDC curves are in conformity to above CV results. Moreover, the initial discharge and charge capacities of CoSe/NC-L composite are 787.9 and 529.6 mA h g^{-1}, respectively, obtaining an initial CE of about 67.2%. And after three cycles, the CE of CoSe/NC-L electrode quickly stabilizes at >98%. The initial irreversible capacity loss is largely due to irreversible phase transition and the formation of SEI, while the subsequent capacity loss corresponds to volume expansion and fragmentation of active materials. Fig. 5c revealed the galvanostatic discharge-charge (GDC) profiles of CoSe/NC-L composite at different current density. According to the peaks of CV curves, all the corresponding plateaus can be observed in the GDC profiles at various current densities, and the distance between oxidation and reduction plateaus (voltage polarization) exhibits slight increase with gradually elevated current density. These results imply an excellent rate capability of CoSe/NC-L composite.

The rate capability and cycling performance of CoSe/NC-L composite are exhibited in Fig. 5d and e. For comparison, the electrochemical performances of CoSe$_x$/NC-L and CoSe$_x$/NC-poly-hedral (as shown in Fig. S6) were also tested. The CoSe/NC-L composite delivers the specific discharge capacities of about 542, 495, 466, 443, 413, and 336 mA h g^{-1} accordingly at the current densities of 0.05, 0.2, 0.5, 1, 2 and 5 A g^{-1}. Once the current density goes back to 0.2 and 0.05 A g^{-1}, the specific capacity returns to 484 and 507 mA h g^{-1}, indicating an excellent electrochemical stability.
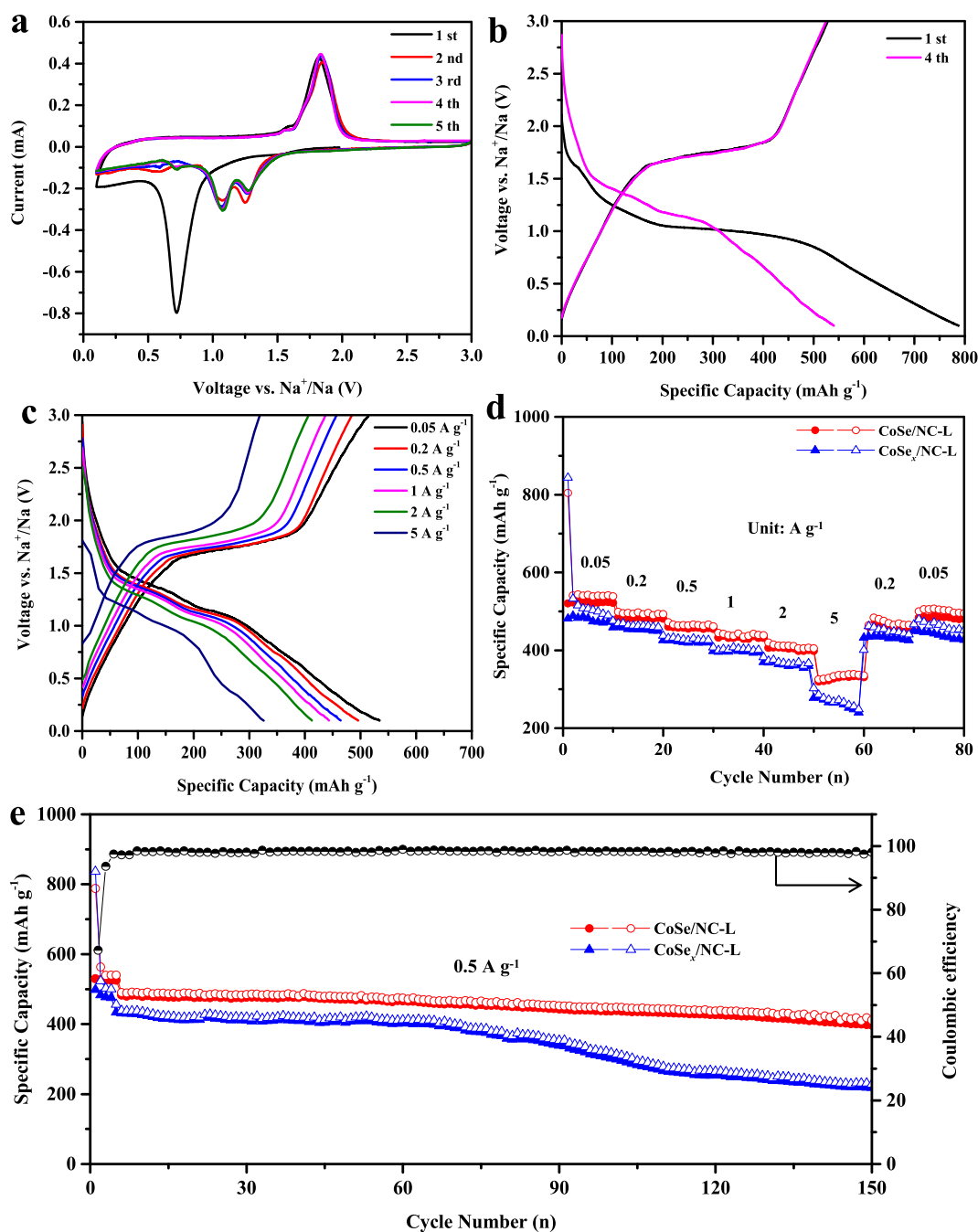
Fig. 5. Electrochemical performances evaluation. a) Representative CV curves for the first, second, third, fourth, and fifth cycles of CoSe/NC-L at a scan rate of 0.1 mV s^{-1} b) GDC profiles of CoSe/NC-L at current density of 0.2 A g^{-1} c) GDC profiles of CoSe/NC-L at various current densities. d) Rate performance of the CoSe/NC-L and CoSe$_x$/NC-L at various current densities. e) Cycling performance of CoSe/NC-L and CoSe$_x$/NC-L at a current density of 0.5 A g^{-1}, and the coulombic efficiency of CoSe/NC-L.

Comparatively, the CoSe$_x$/NC-L electrode shows lower capacity, especially at high current density, which may be correlated with the inferior kinetics caused by the larger particle size and lower selenization degree of CoSe$_x$. For the CoSe$_x$/NC-polyhedral electrode by using the ZIF-67 as precursor, the rate capacity is much worse than that of CoSe$_x$/NC-L hybrid (Fig. S6d), demonstrating the advantages of two-dimensional leaf-like structure. The compared cycling performances was tested in a potential window of 0.1−3.0 V vs Na/Na$^+$ at the current density of 0.5 A g^{-1} (Fig. 5e and S6e). The first four cycles of all these cycling performance were activation process by using the current density of 0.2 A g^{-1}. The specific capacity of the CoSe$_x$/NC-polyhedral decreases quickly from

480 mA h g^{-1} to 70 mA h g^{-1} after 70 cycles (Fig. S6d). Similarly, CoSe$_x$/NC-L hybrid starts to suffer from severe capacity degradation after 80 cycles. In contrast, CoSe/NC-L composite delivers a specific capacity of 397 mAh g^{-1} even after 150 cycles, which shows significantly enhanced cycling stability. In addition, the capacity decay of CoSe$_x$/NC-L and CoSe$_x$/NC-polyhedral are accompanied by a gradually decrease of coulombic efficiency (Fig. S6e, f). It is proposed that the cyclic failure of CoSe material is correlated with the coulombic efficiency (CE), which is influenced by the morphology and structure. Obviously, the ultrafine CoSe nano-crystallites are mainly wrapped into CN matrix, which could alleviate the stresses from volume changes, thus the improvement of CE and cyclic

stability of CoSe/NC-L composite surpassed that of CoSe$_x$/NC-L and CoSe$_x$/NC-polyhedral.

To understand the superior electrochemical performance of CoSe/NC-L composite, its reaction kinetics was studied by CV and EIS measurements. As displayed in Fig. 6a, when the scan rate ranges from 0.2 to 2 mV s^{-1}, all the CV curves of oxidation-reduction process present well-defined peaks, indicating the satisfactory reaction reversibility. The area inside a CV curve represents the capacity that can derive from diffusion-controlled process and pseudo-capacitive behavior [45]. The corresponding charge/discharge mechanism can be determined according to the logarithmic linear relationship of scan rate (v) and peak current (i) as follows:

$$\log(i) = \log(a) + b \log(v) \tag{2}$$

Where slope b of 0.5 means a diffusion-controlled process, and b-value of 1.0 implies a pseudo-capacitive behavior [46–48]. According to the CV curves of CoSe/NC-L composite, the b values of anodic peak and cathodic peak were fitted to be 0.8 and 0.78, respectively (Fig. 6b), implying that the charge/discharge process of CoSe/NC-L is dominated by the pseudo-capacitive behavior. Furthermore, the contribution ratio of the pseudo-capacitive behavior at various scan rates can be quantitatively calculated by the following equation:
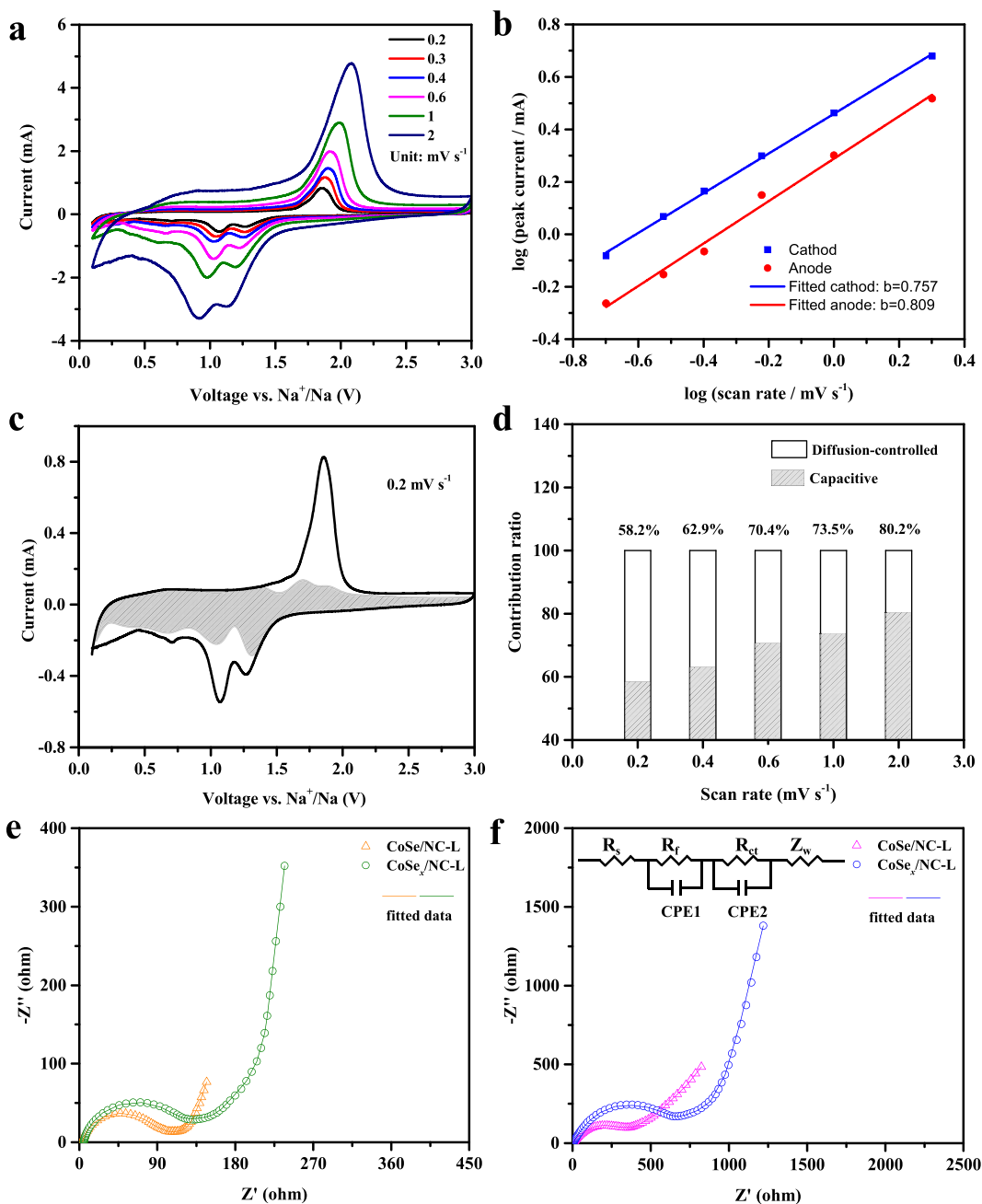
Fig. 6. Kinetics investigation of the electrochemical behavior towards Na$^+$ for the CoSe/NC-L composite. (a) CV curves at different scan rates. (b) Determination of the b-value according to peak current and scan rate. (c) Separation of the capacitive and diffusion currents in CoSe/NC-L at a scan rate of 0.2 mV s^{-1}. (d) Contribution ratio of the capacitive and diffusion behaviors at different scan rate. (e) Nyquist plots of CoSe/NC-L and CoSe$_x$/NC-L before cycling. (f) Nyquist plots of two samples after 100 cycles.

$$i(v) = k_1 v + k_2 v^{1/2} \tag{3}$$

In a voltage window of 0.1—3.0 V, 58.2% of total capacity is assigned to pseudo-capacitive behavior at a scan rate of 0.2 mV s^{-1} (Fig. 6c). As the scan rate increases, the contribution ratio of capacitive process increasingly dominates the total capacity (Fig. 6d). Pervious study [49] demonstrates that active materials with smaller size usually offer a greater proportion of capacitive behavior, thus ultrafine size features favorable for a superior sodium storage performance at high rates. The EIS results further reveal the fast redox reaction happens on the surface of CoSe/NC-L. As shown in Fig. 6e and f, the Nyquist plots of CoSe/NC-L and CoSe$_x$/NC-L consist of a semicircle followed by a slope line, followed with a diffusion drift. It can be analyzed based on an equivalent circuit inset in Fig. 6f, where R$_f$ and R$_{ct}$ are the contact resistance and the charge-transfer resistance at the electrode/electrolyte interface [44], while Z$_w$ is the Warburg impedance associated with Na ions diffusion. The fitting results are given in Table S2. Before cycling, the resistances of CoSe/NC-L are a little smaller than that of CoSe$_x$/NC-L. The CoSe/NC-L contains relatively smaller nanoparticles and higher N-doped carbon matrix, which is responsible for the reduced resistance. After 150 cycles, the R$_f$ and R$_{ct}$ values of CoSe/NC-L both increased due to the pulverization of electrode and formation of SEI film during the repeated Na$^+$ insertion/desertion process. Nevertheless, the CoSe/NC-L composites exhibited much smaller resistances (R$_f$ = 43 Ω, R$_{ct}$ = 308 Ω) than those of CoSe$_x$/NC-L (R$_f$ = 72 Ω, R$_{ct}$ = 681 Ω), which is ascribed to the minor pulverization and stabilized SEI in the CoSe/NC-L electrode. The ability of Na ion transport in electrode material can be estimated by the ion diffusion coefficient (D$_{Na}^+$), which plays crucial role on the electrochemical performance of batteries [50]. The related calculation details were displayed in Fig. S7 and supplement information. According to EIS data, the D$_{Na}^+$ of CoSe/CN-L and CoSe$_x$/CN-L are about 1.67×10^{-15} cm^2 s^{-1} and 1.08×10^{-15} cm^2 s^{-1} for the 150th cycle, respectively, further demonstrating the enhanced sodium ions transport in CoSe/CN-L. Therefore, CoSe/NC-L composite demonstrates enhanced kinetic performance and improved cycling stability, highlighting the structural advantages of ultrafine CoSe and two-dimensional leaf-like matrix.

The SEM observation and corresponding EDS of CoSe/NC-L after 100 cycles were conducted. As shown in Fig. S8a, the CoSe/NC-L composite still retain the 2D sheet structure, even though some aggregations and thin film can be observed. The fine structural retention of CoSe/NC-L is assigned to the favorable stability of 2D carbon matrix and the endurable volume changes of ultrafine CoSe nanoparticles during discharge-charge processes [51]. From the EDS results in Fig. S8b, the cycled CoSe/NC-L contains C, O, Na, Cl, Co and Se elements, indicating the formation of the SEI film on the active material.

The cycle performance of most CoSe-based composites towards sodium ion storage in NaClO$_4$ electrolyte system was reported less than 100 cycles at a high current density. In this work, the unique CoSe/NC-L composite maintains capacity retention of 82.2% even after 150 cycles at 0.5 A g^{-1}, demonstrating a superior cyclic stability. Besides, CoSe/NC-L composite also exhibits excellent rate capability, as shown in Fig. S9. The outstanding electrochemical performance of CoSe/NC-L composite is attributed to the synergistic effect of ultrafine nanoparticles and two-dimensional CN matrix. Firstly, the ultrafine CoSe nano-crystallites derived from nano-sized Se contribute to highly electrochemical activity and fast reaction kinetics for Na ions storage, generating excellent rate performance. Secondly, nitrogen doping endows the two-dimensional carbon matrix with good electrical conductivity, which is advantageous to electronic transport. Meanwhile, the two-

dimensional structure is beneficial to the rapid contact between the matrix and the electrolyte, forming a stable SEI layer for high initial coulombic efficiency. Finally, compared to the exposure of coarsened CoSe$_x$, ultrafine CoSe nano-crystallites are more prone to be encapsulated into two-dimensional matrix, which could effectively accommodate the volume change and pulverization of CoSe nanoparticles and restrain the formation of unstable SEI layers upon cycling, thus delivering high cyclic stability, and coulombic efficiency. Therefore, CoSe/NC-L composite demonstrates superior kinetic performance, cyclic stability, and coulombic efficiency and could be used as high-performance anode materials for SIBs.

4. Conclusions

In summary, a two-dimensional leaf-like composite of ultrafine CoSe nano-crystallites and N-doped carbon matrix was fabricated via a one-pot selenization process. The ultrafine CoSe nano-crystallites (~11 nm) were in-situ formed in the nitrogen-doped carbon matrix during high-temperature reaction of ZIF-L and nano-sized selenium. For comparison, the micro-sized selenium source resulted in an exposure of coarsened CoSe/Co$_9$Se$_8$ mixed crystals (~31 nm) on the surface of CN matrix, obtaining CoSe$_x$/CN-L hybrids. As the anode materials for NIBs, the CoSe/NC-L composite demonstrates superior reaction kinetics and coulombic efficiency, achieving an excellent rate performance and cyclic stability due to the synergistic effect of ultrafine CoSe and encapsulation into two-dimensional NC matrix. This work opens up possibilities for the reasonable design of various selenide materials in electrochemical applications, such as Na/Li ions batteries or electrochemical catalysis.

Appendix A. Supplementary data

Supplementary data to this article can be found online at https://doi.org/10.1016/j.electacta.2018.10.012.

References

[1] J.M. Tarascon, M. Armand, Issues and challenges facing rechargeable lithium batteries, Nature 414 (2001) 171—179.
[2] M. Armand, J.M. Tarascon, Building better batteries, Nature 451 (2008) 652—657.
[3] V. Palomares, P. Serras, I. Villaluenga, K.B. Hueso, J. Carreterogonzález, T. Rojo, Na-ion batteries, recent advances and present challenges to become low cost energy storage systems, Energy Environ. Sci. 5 (2012) 5884—5901.
[4] S.Y. Hong, Y. Kim, Y. Park, A. Choi, N.-S. Choi, K.T. Lee, Charge carriers in rechargeable batteries: Na ions vs. Li ions, Energy Environ. Sci. 6 (2013) 2067—2081.
[5] R. Alcántara, J.M. Jiménez-Mateos, P. Lavela, J.L. Tirado, Carbon black: a promising electrode material for sodium-ion batteries, Electrochem. Commun. 3 (2001) 639—642.
[6] B. Jache, P. Adelhelm, Use of graphite as a highly reversible electrode with superior cycle life for sodium-ion batteries by making use of co-intercalation

phenomena, Angew. Chem. 53 (2014) 10169—10173.

[7] Y. Xu, Y. Zhu, Y. Liu, C. Wang, Electrochemical performance of porous carbon/tin composite anodes for sodium-ion and lithium-ion batteries, Adv. Energy Mater. 3 (2013) 128—133.

[8] Z. Liu, X.Y. Yu, X.W. Lou, U. Paik, Sb@C coaxial nanotubes as a superior long-life and high-rate anode for sodium ion batteries, Energy Environ. Sci. 9 (2016) 2314—2318.

[9] X. Wang, Z. Yang, C. Wang, L. Ma, C. Zhao, J. Chen, X. Zhang, M. Xue, Auto-generated iron chalcogenide microcapsules ensure high-rate and high-capacity sodium-ion storage, Nanoscale 10 (2018) 800—806.

[10] F. Niu, J. Yang, N. Wang, D. Zhang, W. Fan, J. Yang, Y. Qian, MoSe2-Covered N,P-Doped carbon nanosheets as a long-life and high-rate anode material for sodium-ion batteries, Adv. Funct. Mater. 27 (2017), 1700522.

[11] X. Wang, D. Kong, X.H. Zhi, W. Ye, Y.Y. Hui, Nontopotactic reaction in highly reversible sodium storage of ultrathin Co9Se8/rGO hybrid nanosheets, Small 13 (2017), 1603980.

[12] H. Fan, H. Yu, X. Wu, Y. Zhang, Z. Luo, H. Wang, Y. Guo, S. Madhavi, Q. Yan, Controllable preparation of square nickel chalcogenide (NiS and NiSe2) nanoplates for superior Li/Na ion storage properties, ACS Appl. Mater. Interfaces 8 (2016) 25261—25267.

[13] Q. Tang, Y. Cui, J. Wu, D. Qu, A.P. Baker, Y. Ma, X. Song, Y. Liu, Ternary tin selenium sulfide (SnSe0.5S0.5) nano alloy as the high-performance anodes for lithium-ion and sodium-ion batteries, Nanomater. Energy 41 (2017) 377—386.

[14] K. Zhang, Z. Hu, X. Liu, Z. Tao, J. Chen, FeSe2 microspheres as a high-performance anode material for Na-ion batteries, Adv. Mater. 27 (2015) 3305—3309.

[15] Q.H. Wang, K. Kalantarzadeh, A. Kis, J.N. Coleman, M.S. Strano, Electronics and optoelectronics of two-dimensional transition metal dichalcogenides, Nat. Nanotechnol. 7 (2012) 699—712.

[16] Q. Li, H. Liu, Z. Yao, J. Cheng, T. Li, Y. Li, C. Wolverton, J. Wu, V.P. Dravid, Electrochemistry of selenium with sodium and lithium: kinetics and reaction mechanism, ACS Nano 10 (2016) 8788.

[17] G.D. Park, Y.C. Kang, One-pot synthesis of CoSex—rGO composite powders by spray pyrolysis and their application as anode material for sodium-ion batteries, Chemistry 22 (2016) 4140—4146.

[18] Z. Zhang, X. Yang, Y. Fu, K. Du, Ultrathin molybdenum diselenide nanosheets anchored on multi-walled carbon nanotubes as anode composites for high performance sodium-ion batteries, J. Power Sources 296 (2015) 2—9.

[19] H. Liu, H. Guo, B. Liu, M. Liang, Z. Lv, K.R. Adair, X. Sun, Few-layer MoSe2 nanosheets with expanded (002) planes confined in hollow carbon nanospheres for ultrahigh-performance Na-ion batteries, Adv. Funct. Mater. (2018), 1707480.

[20] Y. Zhang, A. Pan, L. Ding, Z. Zhou, Y. Wang, S. Niu, S. Liang, G. Cao, Nitrogen-doped yolk-shell structured CoSe/C dodecahedra for high-performance sodium-ion batteries, ACS Appl. Mater. Interfaces 9 (2017) 3624—3633.

[21] S.-K. Park, J.K. Kim, Y.C. Kang, Excellent sodium-ion storage performances of CoSe2 nanoparticles embedded within N-doped porous graphitic carbon nanocube/carbon nanotube composite, Chem. Eng. J. 328 (2017) 546—555.

[22] J. Li, D. Yan, T. Lu, Y. Yao, L. Pan, An advanced CoSe embedded within porous carbon polyhedra hybrid for high performance lithium-ion and sodium-ion batteries, Chem. Eng. J. 325 (2017) 14—24.

[23] S.K. Park, K.K. Jin, C.K. Yun, Metal—organic framework-derived CoSe2/(NiCo) Se2 box-in-box hollow nanocubes with enhanced electrochemical properties for sodium-ion storage and hydrogen evolution, J. Mater. Chem. 5 (2017) 18823—18830.

[24] Y. Zhang, A. Pan, L. Ding, Z. Zhou, Y. Wang, S. Niu, S. Liang, G. Cao, Nitrogen-doped yolk-shell structured CoSe/C dodecahedra for high-performance sodium-ion batteries, ACS Appl. Mater. Interfaces 9 (2017) 3624—3633.

[25] X. Xu, J. Liu, J. Liu, L. Ouyang, R. Hu, H. Wang, L. Yang, M. Zhu, A general metal-organic framework (MOF)-Derived selenidation strategy for in situ carbon-encapsulated metal selenides as high-rate anodes for Na-ion batteries, Adv. Funct. Mater. 28 (2018), 1707573.

[26] Y.N. Ko, S.H. Choi, Y.C. Kang, Hollow cobalt selenide microspheres: synthesis and application as anode materials for Na-ion batteries, ACS Appl. Mater. Interfaces 8 (2016) 6449—6456.

[27] R. Chen, J. Yao, Q. Gu, S. Smeets, C. Baerlocher, H. Gu, D. Zhu, W. Morris, O.M. Yaghi, H. Wang, A two-dimensional zeolitic imidazolate framework with a cushion-shaped cavity for CO2 adsorption, Chem. Commun. 49 (2013) 9500—9502.

[28] Y. Guo, K. Xu, C. Wu, J. Zhao, Y. Xie, Surface chemical-modification for engineering the intrinsic physical properties of inorganic two-dimensional nanomaterials, Chem. Soc. Rev. 44 (2015) 637—646.

[29] T. Zhou, W.K. Pang, C. Zhang, J. Yang, Z. Chen, H.K. Liu, Z. Guo, Enhanced sodium-ion battery performance by structural phase transition from two-dimensional hexagonal-SnS2 to orthorhombic-SnS, ACS Nano 8 (2014) 8323—8333.

[30] X. Li, Y. Feng, M. Li, W. Li, H. Wei, D. Song, Smart hybrids of Zn2GeO4 nanoparticles and ultrathin g-C3N4 layers: synergistic lithium storage and excellent electrochemical performance, Adv. Funct. Mater. 25 (2016) 6858—6866.

[31] P. Ge, H. Hou, X. Cao, S. Li, G. Zhao, T. Guo, C. Wang, X. Ji, Multidimensional evolution of carbon structures underpinned by temperature-induced intermediate of chloride for sodium-ion batteries, Adv. Sci. 5 (2018), 1800080.

[32] S. Biniak, G. Szymański, J. Siedlewski, A. Świątkowski, The characterization of activated carbons with oxygen and nitrogen surface groups, Carbon 35 (1997) 1799—1810.

[33] Z. Yang, M. Xu, Y. Liu, F. He, F. Gao, Y. Su, H. Wei, Y. Zhang, Nitrogen-doped, carbon-rich, highly photoluminescent carbon dots from ammonium citrate, Nanoscale 6 (2014) 1890.

[34] W. Xia, J. Zhu, W. Guo, L. An, D. Xia, R. Zou, Well-defined carbon polyhedrons prepared from nano metal—organic frameworks for oxygen reduction, J. Mater. Chem. 2 (2014) 11606—11613.

[35] W. Li, X. Gao, D. Xiong, F. Wei, W.G. Song, J. Xu, L. Liu, Hydrothermal synthesis of monolithic Co3Se4 nanowire electrodes for oxygen evolution and overall water splitting with high efficiency and extraordinary catalytic stability, Adv. Energy Mater. 7 (2017), 1602579.

[36] H.-W. Chen, C.-W. Kung, C.-M. Tseng, T.-C Wei, N. Sakai, S. Morita, M. Ikegami, T. Miyasaka, K.-C. Ho, Plastic based dye-sensitized solar cells using Co9S8 acicular nanotube arrays as the counter electrode, J. Mater. Chem. 1 (2013) 13759—13768.

[37] L. Han, W. Qin, J. Zhou, J. Jian, S. Lu, X. Wu, G. Fan, P. Gao, B. Liu, Chemical grafting of Co9S8 onto C60 for hydrogen spillover and storage, Nanoscale 9 (2017) 5141—5147.

[38] J. Mujtaba, H. Sun, G. Huang, Y. Zhao, H. Arandiyan, G. Sun, S. Xu, J. Zhu, Co9S8 nanoparticles encapsulated in nitrogen-doped mesoporous carbon networks with improved lithium storage properties, RSC Adv. 6 (2016) 31775—31781.

[39] D. Kong, H. Wang, Z. Lu, Y. Cui, CoSe2 nanoparticles grown on carbon fiber paper: an efficient and stable electrocatalyst for hydrogen evolution reaction, J. Am. Chem. Soc. 136 (2014) 4897—4900.

[40] Q. Liu, J. Shi, J. Hu, A.M. Asiri, Y. Luo, X. Sun, CoSe2 nanowires array as a 3D electrode for highly efficient electrochemical hydrogen evolution, ACS Appl. Mater. Interfaces 7 (2015) 3877—3881.

[41] M.A. Nabar, S.V. Paralkar, Thermal decomposition of some divalent metal selenates, Thermochim. Acta 11 (1975) 187—196.

[42] H. Hu, J. Zhang, B. Guan, X.W. Lou, Unusual formation of CoSe@carbon nanoboxes, which have an inhomogeneous shell, for efficient lithium storage, Angew. Chem. Int. Ed. 55 (2016) 9514—9518.

[43] Y. Zhang, A. Pan, Y. Wang, X. Cao, Z. Zhou, T. Zhu, S. Liang, G. Cao, Self-templated synthesis of N-doped CoSe2/C double-shelled dodecahedra for high-performance supercapacitors, Energy Storage Mater. 8 (2017) 28—34.

[44] X. Li, G. Wu, X. Liu, W. Li, M. Li, Orderly integration of porous TiO2 (B) nanosheets into bunchy hierarchical structure for high-rate and ultralong-lifespan lithium-ion batteries, Nanomater. Energy 31 (2017) 1—8.

[45] P. Ge, C. Zhang, H. Hou, B. Wu, L. Zhou, S. Li, T. Wu, J. Hu, L. Mai, X. Ji, Anions induced evolution of Co3X4 (X = O, S, Se) as sodium-ion anodes: the influences of electronic structure, morphology, electrochemical property, Nanomater. Energy 48 (2018) 617—629.

[46] Z. Ali, T. Tang, X. Huang, Y. Wang, M. Asif, Y. Hou, Cobalt selenide decorated carbon spheres for excellent cycling performance of sodium ion batteries, Energy Storage Mater. 13 (2018) 19—28.

[47] C. Chen, Y. Wen, X. Hu, X. Ji, M. Yan, L. Mai, P. Hu, B. Shan, Y. Huang, Na+ intercalation pseudocapacitance in graphene-coupled titanium oxide enabling ultra-fast sodium storage and long-term cycling, Nat. Commun. 6 (2015) 6929.

[48] K. Zhang, M. Park, L. Zhou, G.H. Lee, W. Li, Y.M. Kang, J. Chen, Urchin-like CoSe2 as a high-performance anode material for sodium-ion batteries, Adv. Funct. Mater. 26 (2016) 6728—6735.

[49] J. Wang, J. Polleux, A. James Lim, B. Dunn, Pseudocapacitive contributions to electrochemical energy storage in TiO2 (Anatase) nanoparticles, J. Phys. Chem. C 111 (2007) 14925—14931.

[50] P. Ge, H. Hou, X. Ji, Z. Huang, S. Li, L. Huang, Enhanced stability of sodium storage exhibited by carbon coated Sb2S3 hollow spheres, Mater. Chem. Phys. 203 (2017).

[51] G. Fang, Z. Wu, J. Zhou, C. Zhu, X. Cao, T. Lin, Y. Chen, C. Wang, A. Pan, S. Liang, Observation of pseudocapacitive effect and fast ion diffusion in bimetallic sulfides as an advanced sodium-ion battery anode, Adv. Energy Mater. 8 (2018), 1703155.